Improved design of large wind turbine blades of fibre composites (Phase 2) - Summary Report

Sørensen, Bent F.; Branner, K.; Stang, H.; Jensen, H.M.; Lund, E.; Jacobsen, T.K.; Halling, K.M.

Publication date:
2005

Document Version
Publisher's PDF, also known as Version of record

RISØ

Risø-R-1526(EN)

Improved design of large wind turbine blades of fibre composites (Phase 2) - Summary Report

Bent F. Sørensen[#], Kim Branner*, Henrik Stang[$], Henrik M. Jensen[$], Erik Lund[£], Torben K. Jacobsen[¤] and Kaj M. Halling[+]

Risø National Laboratory
Roskilde
Denmark
August 2005

Author: Bent F. Sørensen[#], Kim Branner[*], Henrik Stang[$], Henrik M. Jensen[$], Erik Lund[£], Torben K. Jacobsen[¤] and Kaj M. Halling[+]
Title: Improved design of large wind turbine blades of fibre composites (Phase 2) - Summary Report
Department: [#]Materials Research Department, Risø National Laboratory, 4000 Roskilde, Denmark; *Wind Energy Department, Risø National Laboratory, 4000 Roskilde, Denmark; [§]Department of Civil Engineering, The Technical University of Denmark, 2800 Lyngby, Denmark; [$]Department of Building Technology and Structural Engineering, Aalborg University, 9000 Aalborg, Denmark; [£]Institute of Mechanical Engineering, Aalborg University, 9220 Aalborg East, Denmark; [¤]LM Glasfiber A/S, 6640 Lunderskov, Denmark; [+]Vestas Wind Systems A/S, 6950 Ringkøbing, Denmark

Risø-R-1526(EN)
August 2005

Abstract (max. 2000 char.):

The major results of Phase 2 of a project concerning the development of new design methods for wind turbine blades are summarised. Finite element models were used for studying the buckling behaviour of a box girder, tested to failure in Phase 1 of this project. The deformation behaviour of a box girder section subjected to transverse forces was investigated experimentally and by modelling. Buckling-driven delamination of planar specimens was studied on experimentally and by modelling. A novel approach was proposed for the determination of mixed mode cohesive laws for large-scale crack bridging problems. The normal and shear stresses of the cohesive laws were obtained from data of the fracture resistance and the normal and tangential displacements of the cohesive zone. Delamination of a thin layer bonded to an elastic substrate close to corners and edges was also analysed. Results for the shape of the interface crack front and critical stress for steady-state delamination were obtained.

ISSN 0106-2840
ISBN 87-550-3462-4

Contract no.:
1363/03-0006

Group's own reg. no.:
1615063-00

Sponsorship:
Danish Energy Authority under the Ministry of Economics and Business Affairs

Pages: 38
Tables:
References:

Risø National Laboratory
Information Service Department
P.O.Box 49
DK-4000 Roskilde
Denmark
Telephone +45 46774004
bibl@risoe.dk
Fax +45 46774013
www.risoe.dk

Contents

Preface

This summary-report contains a sort summary of the activities of the project "Improved design for large wind turbine blades, Phase 2)", partially supported by the Danish Energy Authority under the Ministry of Economics and Business Affairs through an EFP2003-fund (journal no. 1363/03-0006). The project ran from year 2003 to 2005. The participants in the project were: The Materials Research Department, Risø National Laboratory (project leader), The Wind Energy Department, Risø National Laboratory, Department of Civil Engineering, The Technical University of Denmark, the Department of Building Technology and Structural Engineering, Aalborg University, the Institute of Mechanical Engineering, Aalborg University, LM Glasfiber A/S and Vestas Wind Systems A/S. The project was a continuation of the project Improved design for large wind turbine blades, based on studies of scale-effects (Phase 1)", partially supported by the Danish Energy Authority under the Ministry of Economics and Business Affairs through a EFP2001-fund (journal no. 1363/01-01-0007).

1 Introduction

1.1 Background

The rapid up-scaling of the sizes of wind turbines leads to the requirement for better design criteria, since it becomes essential to save material in order to reduce weight (gravitational forces) and reduce costs. Wind turbine blades are the largest rotating component in a wind turbine, so they weight savings here are beneficial for rest of the turbine.

The load carrying parts of wind turbine blades are made of fibre composites. During the last 25 years, methods for determination of *loads* on a wind turbine have been developed to a very advance stage. The design criteria with *strength* of materials and structures have not been improved in the same manner. For instance, the current design criteria do not cover many of the possible failure modes. To compensate for material variation and for uncertainties related to the models for strength and lifetime predictions, the current design approaches use relative large partial coefficients (Christensen *et al*., 2000). Furthermore, wind turbine blades must pass a detailed full-scale test to be certified.

Partial coefficients cover uncertainties associated with the design methods in use. Usually, wind turbine blades are modelled as being 'perfect', while real blades contain imperfections, such as geometrical deviations, flaws and material variation. Consequently, it must be possible to reduce the size of the partial coefficients by developing failure criteria that takes these uncertainties into account.

The idea pursued here is to set up models for the different failure modes that can develop in wind turbine blade as a result of imperfections. An example of the idea is shown in Fig. 1.1. Here, a global model of a wind turbine blade is coupled to a mode of a buckling-driven delamination. Then, it becomes possible to determine load at which the delamination begins to grow as a function of the size and position of the delamination. Thus, it becomes possible to *quantify* effects of the imperfections and uncertainties that previously were covered by partial coefficients can be eliminated.

1.2 Purpose

The long-term goal is to develop *general approaches* and *generic models* for each possible failure modes, so that the material properties can be fully utilised and the structural design can be optimised. The new design methods will enable the wind turbine industry to improve their design details and their choice of materials.

The specific problems investigated in this project (Phase 2) are failure in composite structures under compressive loading, strength of adhesive joints under mixed mode (from pure peel to pure shear) loading, and delamination of laminates.

This report is a summary report of the project, and contains only a brief presentation of the major results. More details can be found in the publications made throughout the project. These publications are listed in the end of this report.

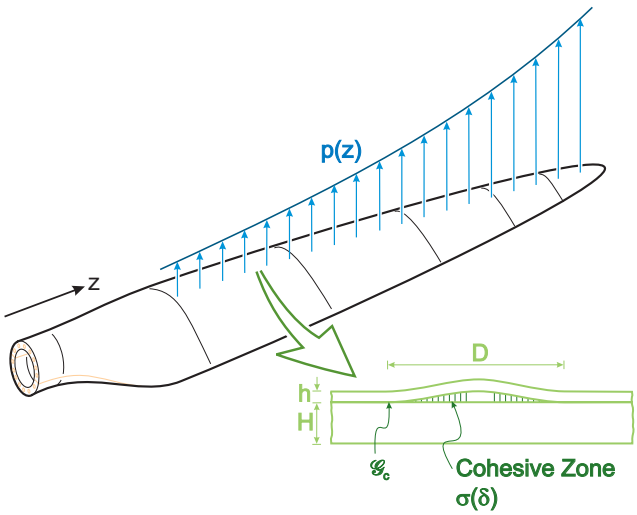

Figure 1.1: Illustration of an analysis of buckling-driven delamination in a wind turbine blade by a combination of a global and a local model. By the use of the local model, it is the size, D, and depth, h, of the delamination, as well as the fracture properties (fracture energy of the crack tip and the cohesive law, $\sigma(\delta)$, describing fibre bridging) that controls at which load level the delamination extends.

2 Structural instability occurrences in a wind turbine blade

2.1 Experimental investigations

An overall fracto-graphic analysis and evaluation of the full-scale experiment of the 25 meters V52 wind turbine blade (from Vestas Wind Systems A/S) that was tested to failure in Phase 1. The purpose was to determine the main cause of failure and plausible failure sequence. A preliminary test report has been written of the observed and measured events during testing (Overgaard, 2004). This technical report will give basis for a paper (Overgaard and Lund, 2005B), concerning the assessment of structural collapse of the full-scale experiment.

2.2 Finite element models

A general pre-processing program for generating finite element models of Vestas wind turbine blades has been established. The input is a CAD model of the geometry and ascii text files defining the laminate lay-up together with information about the discretization wanted, and the output is FE models that can be used by several different finite element solvers.

The employed finite element models have been tuned based on parametric finite element analyses of the adjacent structural members in order to estimate the most feasible discretization of the blade that is capable of modelling the correct deformation field. This is done with the use of benchmark shell models and 2D elasticity models as briefly outlined in Overgaard and Lund (2005).

In Overgaard and Lund (2005) design sensitivity analyses of the core material thickness distribution in the web along the length of the blade are studied together with flange angle misalignment under the influence of a geometric imperfection. The paper also

illustrates the possibility of performing design optimization on the 25 meters test blade based on a local criterion of minimizing the maximum strain in a geometrically nonlinear analysis. The geometrically nonlinear analysis is performed for predicting the failure of the blade due to local buckling on the suction side (downwind side) of the airfoil. Also the full-scale experiments of the static collapse of the wind turbine blade have been used as reference for verifying the finite element shell model used in this paper.

The previous work will be used in Overgaard and Lund (2005C) for comparison of the observed phenomena during testing and the predictive models in order to obtain knowledge and understanding about the instability of wind turbine blades.

2.3 Synthesis

A synthesis where numerical and experimental data are compared is briefly shown and discussed in Overgaard and Lund (2005A) and is outlined here. The structural collapse of section 3 of the 25 m test blade is located at the maximum Geometric Imperfection Amplitude (GIA) with maximum longitudinal strain, see Figure 1. The epic centre of the buckling mode is located at the Flange Material Transition (FMT), where additional ply-inserts are located, and the Core Material Transition (CMT), which is at the core material thickness transition where the core thickness is halved. The positions FMT and CMT are located at the same distance from the root.

When the blade buckles locally in the suction side of the aerofoil at the FMT and CMT, it triggers high strain levels at the GIA, which ultimately causes a progressive failure of the blade. The comparison in Fig. 2.1 shows that a longitudinal strain measurement is sufficient to reveal the collapsed section of the blade. Nevertheless it is not sufficient to disclose the buckling critical section of the blade, which is found at the CMT and FMT according to the numerical investigations.

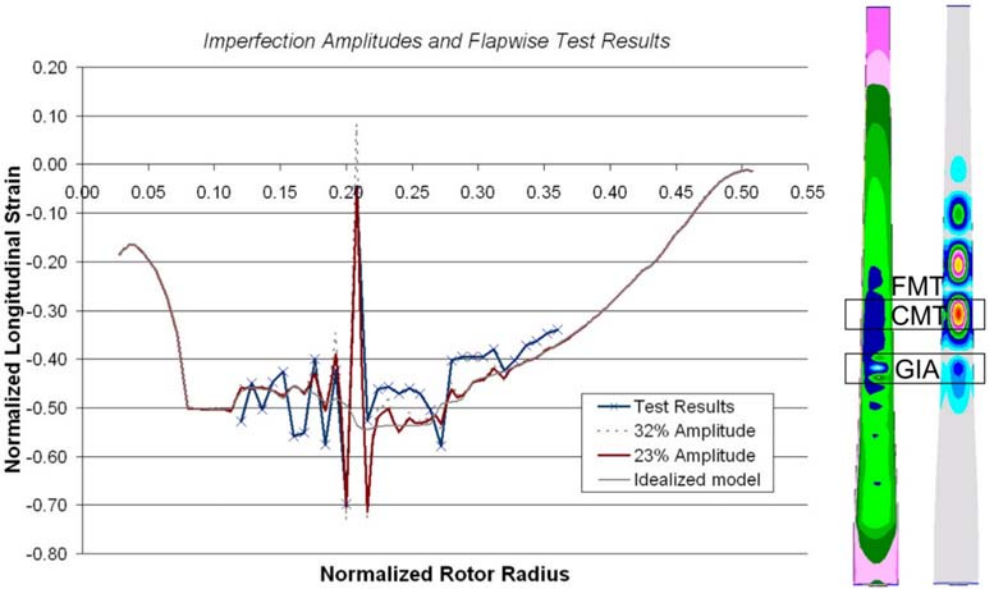

Figure 2.1: Buckling mode and longitudinal strain as a function of distance from root.

The geometric imperfection field is understood to originate from the design and manufacturing of the main spar mandrill, where the cross-section from the round root at the hub to the aerodynamic rectangular box design causes an alternating longitudinal curvature profile, which to some extent matches the strain pattern seen in the static test.

These issues will be investigated further in the forthcoming paper, see Overgaard and Lund (2005C).

The formulation of preliminary design guidelines in connection with the synthesis is too premature in this context, but will be a part of the PhD dissertation.

2.4 Semi- and analytical finite strip models

In addition to the numerical finite element model a semi- and analytical model is being established. The semi- and analytical finite strip program Aalborg University Finite Strip Method (AAUFSM) is used for investigation of structural instability. The program is based on both linear and non-linear theory of elasticity of prismatic thin-walled cross-sections with full ABD-laminate characteristics. The strain-displacement relations allow for an imperfection field in order to simulate the effects of geometric imperfections.

The development of this analysis tool has been on hold for a greater period of time, but will be reinitiated again in the near future. The results of this development will not be a part of the given papers and reports in this section, but will be available in the PhD dissertation.

3 Buckling and compressive strength

3.1 Introduction

Many modern wind turbine blades are constructed with a load-carrying box girder (also called the main spar, see Fig. 3.1) that supports the outer shell. The purpose of the box girder is to give the blade sufficient strength and stiffness, both globally and locally. Globally, the blade should be sufficiently stiff in order not to collide with the tower during operational loading. Locally, the box girder, together with the stiffness of the outer shell, ensures that the shape of the aerodynamic profile is maintained.

The pressure load on the blade results in edgewise and flapwise bending, as well as torsional loading of the blade. The box girder primarily carries the flapwise and torsional loads, while the edgewise bending is carried primarily by strengthening the leading and trailing edges of the aerodynamic profile. In flapwise bending, one side of the box girder is in compression and one side in tension. The compressive loading may cause the flange to fail in buckling. This failure mechanism is expected to be more critical as the size of wind turbine blades is increased.

Large local deflections occur in the transverse direction as the flange starts to buckle and the webs are also taking part in this deformation, see Sørensen *et al*. (2004).

Usually only a small number of shell elements are used in the transverse direction to model the box structure by Finite Element Analysis (FEA). It can therefore be questioned how accurate the obtained results are for strains and stresses in the transverse (*xy*) plane.

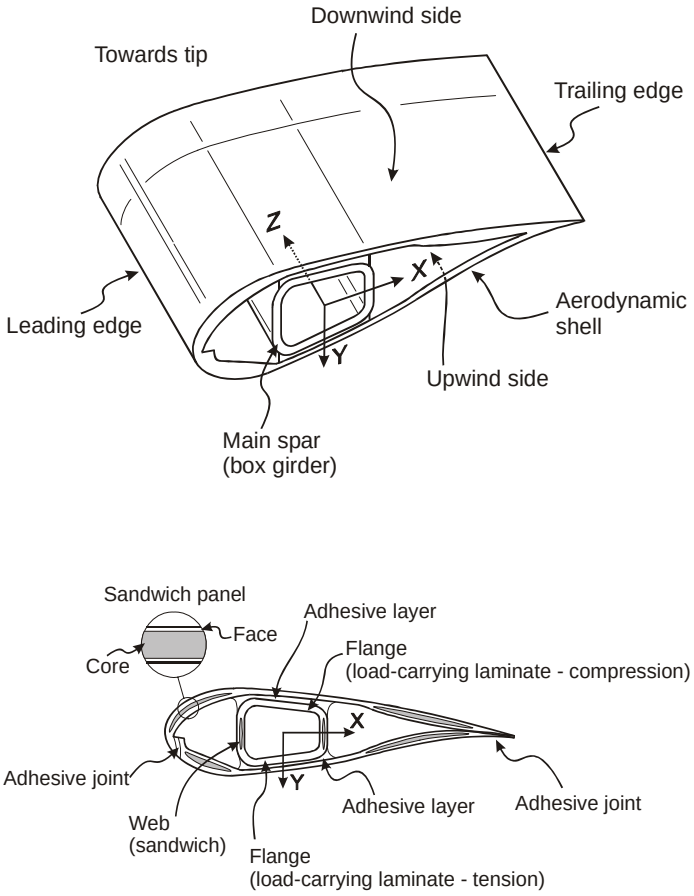

Figure 3.1: Blade structure with definition of terminology. From Sørensen et al. (2004).

It is also well known that the boundary conditions have a great influence on the buckling strength of a panel. For the box girder, the corner stiffness represents the boundary condition of the flange and the accuracy of the modelling of these boundary conditions is questionable, when a small number of shell elements are used in the transverse direction. The purpose of the investigations presented here is to measure transverse properties of a box girder experimentally in order to investigate how well different finite element models predict these transverse properties. Comparison between shell and solid FE-models has previously been done by Pardo & Branner (2005) assuming isotropic material.

3.2 Blade description

The test specimens used in the experiments come from a 25m blade, which is used for the Vestas V52 wind turbine. The box girder extends from the root of the blade to a position close to the tip. The outer shell is mainly designed from aerodynamic considerations and behaves as a secondary structure that transfers the pressure loads on the blade to the box girder. The blade is made mainly using glass fibre/epoxy matrix prepregs. The blade section is shown in Fig. 3.2.

Figure 3.2: Blade section used for cutting out of test specimens.

Table 3.1: Description of specimens used in test.

Test specimen	Depth	Location in blade
1a	104.5 mm	~ R8080
1b	193.5 mm	~ R8550
1c	299.0 mm	~ R8290

3.3 Test procedure

The tests are performed in displacement control using a 250 kN Instron material testing machine. The test setup is shown in Figure 3.3. The upwind side (bottom flange) is supported by two cylinders symmetrical about the midplane. The downwind side (top flange) is loaded by a cylinder in the midplane. Both the support and loading cylinders are slightly angled in order to account for the longitudinal tapering of the box girder. The support cylinders are angled such that the specimen cut planes are vertical.

Two LVDT's are used on the top flange to measure the deflection of the flange relative to the loading line. Two LVDT's measure the outward deflection of the webs. The LVDT's are fixed to the frame of the test machine. During loading the top is fixed and the bottom with the two supports is moving upward with a displacement rate of 2 mm/min. This means that the measuring point of the web LVDT's is moving downward as the load increase. This is taken into account when the results are presented.

Each specimen is equipped with 16 strain gauges. Eight of these are placed at approximately the same location on each specimen, while the other 8 are positioned differently for the 3 specimens.

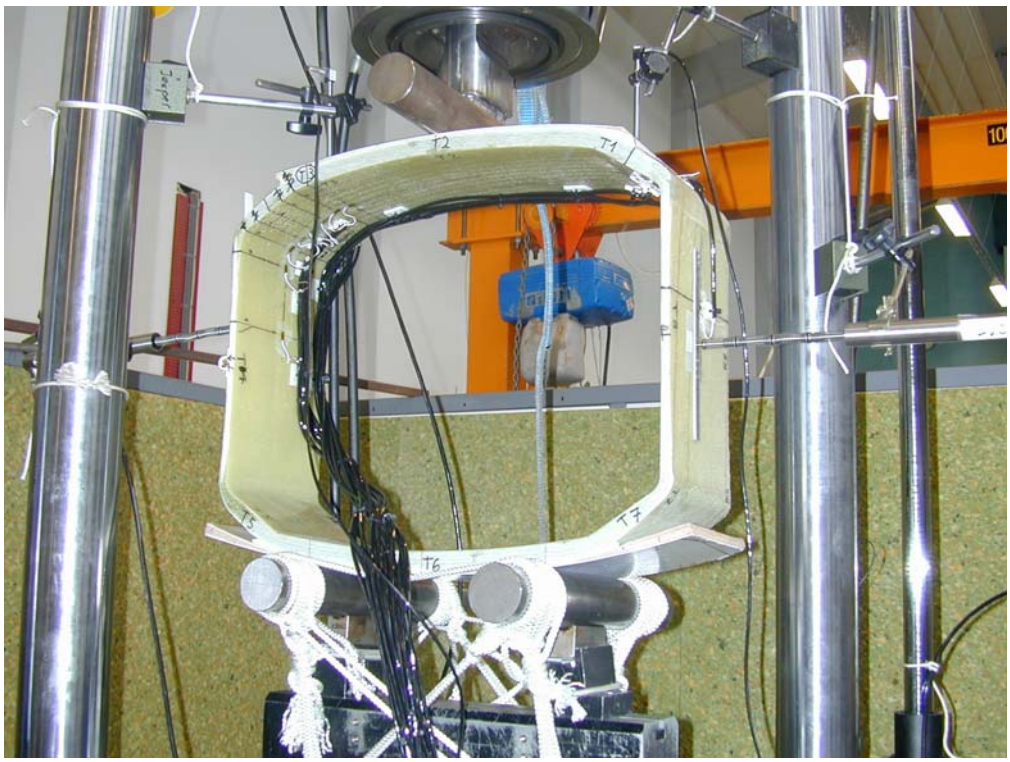

Figure 3.3: Test setup. The top is fixed and the bottom with the two supports is moving upward during loading.

3.4 FE model

The specimen 1b was modelled using MSC Patran and analyzed using MSC Marc. The model is shown in Figure 3.4 and is a 2D-model meshed with approximately 73000 2D-solid elements. The 2D-solid elements possess orthotropic material properties.

The boundary conditions and loading corresponds to the test setup and is shown in Fig. 3.4.

Both linear and non-linear analyses are made using a plane strain formulation with MSC Marc. The non-linear analysis takes geometrical non-linearities into account using a large displacement/small strain formulation. Material non-linearities are not considered.

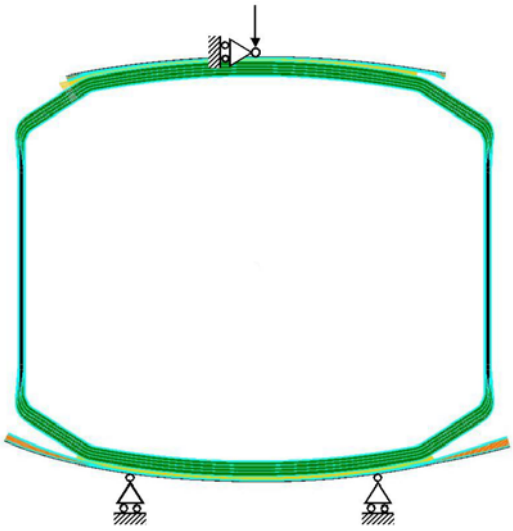

Figure 3.4. 2D solid finite element model with loading and boundary conditions.

The overall deformation (actuator load versus travel) of the test specimens is shown in Fig. 3.5. The load per unit depth is normalised with the maximum failure load per unit depth of the 3 specimens. The deformation is normalised with the height of the specimen. The load-displacement behaviour of the 3 specimens were very similar. The behaviour is linear up to a deformation of approximately 1% of the specimen height. Geometrical non-linearities can explain the behaviour up to approximately 2.2% of deformation. Hereafter material non-linearities seem to be taking over.

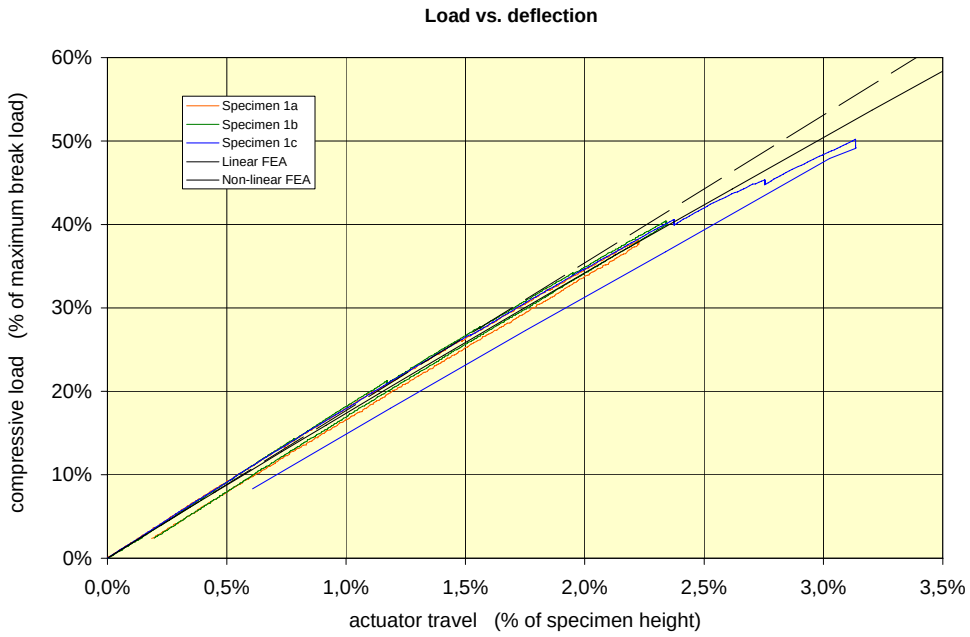

Figure 3.5: Actuator load versus actuator displacement for the 3 specimens. The black lines are from the linear and non-linear finite element analysis.

The displacement of the top flange for 2 of 3 specimens is shown in Fig. 3.6. The position is normalised with the breadth of the specimen such that 0 corresponds to the load point at the centre and 1 corresponds to the end of the flange at the webs. The displacement is normalised with the overall deformation of the specimens. The test results correspond very well with the finite element prediction. It is found that the displacement of the top flange accounts for approximately 68% of the overall displacement of the specimens. The flange behaviour is closer to that of a simply supported beam than that of a clamped beam. It is found that a model consisting of a beam (simple beam theory) with a rotational spring stiffness of 3.5 $(EI/l)_{web}$ at the ends, gives the same deformation as the FE-analysis (E, I and l are the Young's modulus, moment of initia and length of the web respectively). For such a beam**,** zero moment in the flange occur at 90% from the centreline, which corresponds well with the strain gauge measurements, presented in Fig. 3.7.

The deflection of the webs for 2 of 3 specimens is shown in Fig. 3.7. The position is normalised with the height of the webs such that zero corresponds to the centre and ±1 corresponds to the end of the web at the corners. The deflection is normalised with the overall displacement of the specimens. The test results correspond very well with the finite element prediction. The maximum web deflection occur approximately 15% above the centre and the deflection is found to be slightly over half of the overall deformation

of the specimens. Approximately half the web-deformation comes from local deformation of the webs and the other half comes from flattening of the flanges.

The strain gauge results for all 3 specimens are shown in Fig. 3.8 for the inner side. The position is normalised with the inner surface length such that zero corresponds to the centre of the webs and ±1 corresponds to the centre of the top and bottom flanges respectively. The strain is normalised with the height of specimen and overall displacement of the specimens.

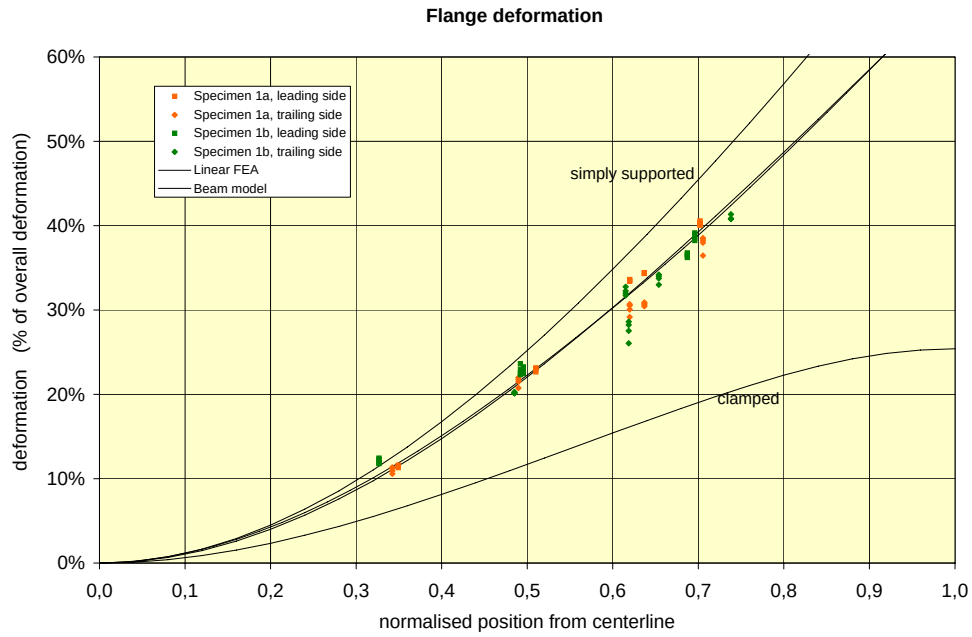

Figure 3.6: Displacement of flange for 2 of the 3 specimens.

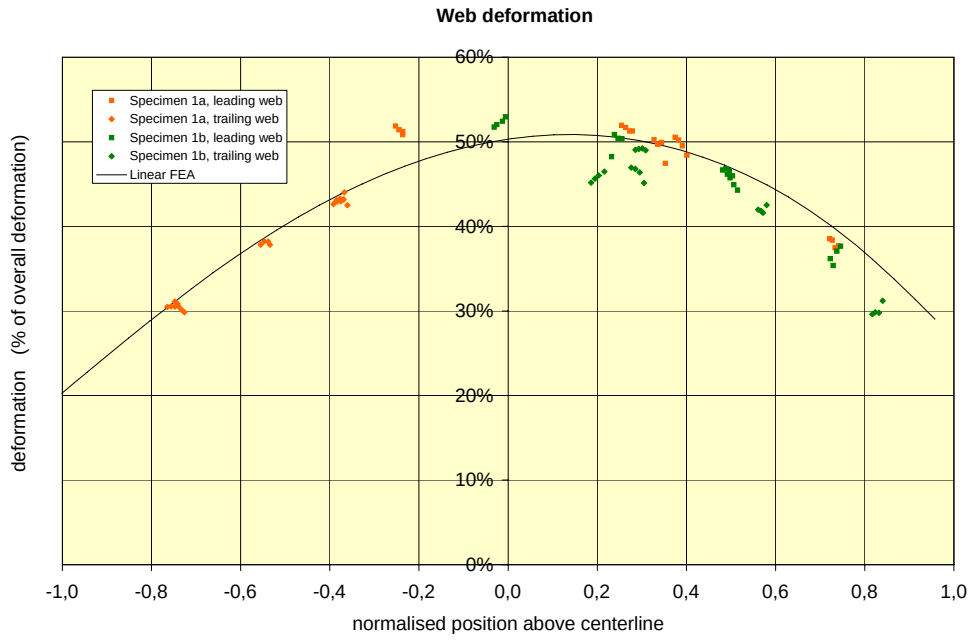

Figure 3.7: Displacement of web for 2 of the 3 specimens.

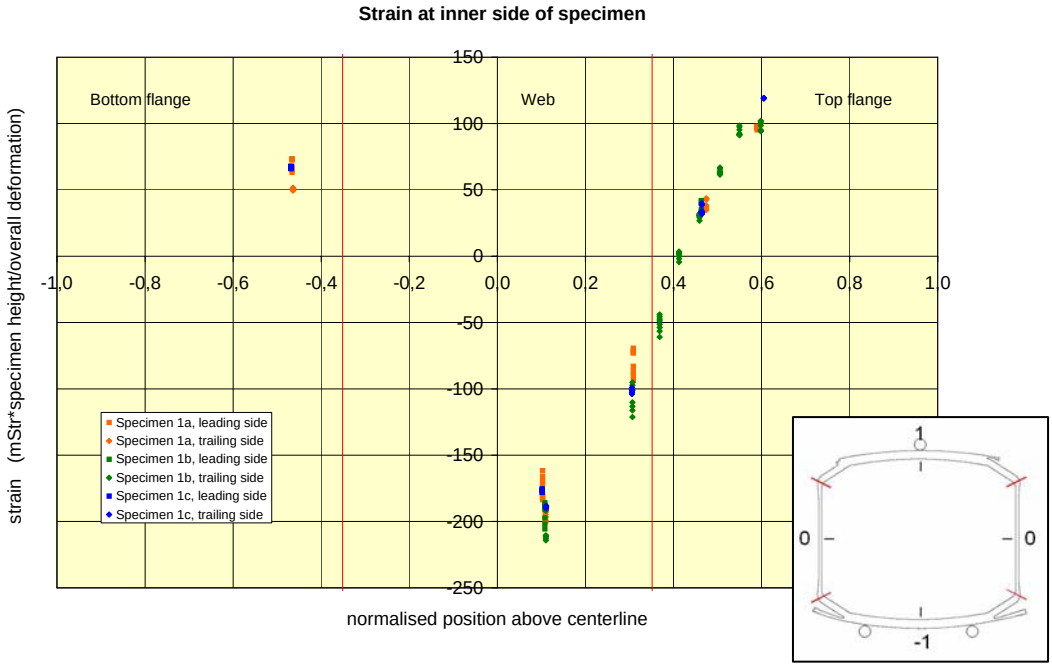

Figure 3.8: Strain gauge measurements on inner side of specimens.

3.5 Conclusions and future work

Three specimens cut from the load carrying box girder of a 25m wind turbine blade was tested and deformations and strains were measured. The specimens have different depths, but only little difference is seen for the measurements. Thus, the results seem to be independent of specimen depth as long as the depth is more than approximately 20% of the specimen height or breadth.

Very good agreement between measurements and FE calculations are found for the deflections, both overall and for the flange and web. The behaviour is linear up to a overall deformation of approximately 1% of the specimen height. Geometrical non-linearities can explain the behaviour up to approximately 2.2% of deformation. Hereafter material non-linearities seem to be taking over. Further analysis of the strains will be performed and published later. The specimens were tested until failure and the results together with numerical predictions will be published later. Further analyses of non-linear effects including material non-linearities are also planned in Phase 3.

4 Buckling-driven delamination: modelling and experiments

4.1 Introduction

Delaminations may be present or may form during service in composite laminates. Extensive analytical and numerical studies have been conducted over the past two decades to calculate the bifurcation loads and to investigate the post-buckling performance of laminates containing interior one-dimensional strip or two-dimensional elliptical delaminations. In a real composite element, an interior delamination may or may not buckle away from the rest of the element depending upon its size, how far below the surface it is located in the element and the level of the local compressive stress field. It may not buckle at all if it is very small in size, or if the delamination is situated

deep in the interior of the laminate or if the magnitude of the local compressive stress is small. If it buckles, then the post-buckling response will depend not only on its size and location below the surface and the level of the local compressive stress, but also on the critical energy release rate of the composite material for the mode mixity present at the delamination front. In the post-buckled state, if the local compressive stress is increased, the delamination may simply continue to deform or it may grow in size if the energy release rate exceeds the critical value for the given mode mixity. The growth is however likely to be sub-critical because of the *R*-curve behaviour of the laminate material.

In this work the pre- and post-buckling response of a strip delamination in a composite laminate is thoroughly examined and guidelines developed for assessing whether or not it poses a threat to the safe operation of the composite laminate. By a strip delamination is meant a one-dimensional delamination across the entire width of the laminate such that it is constrained only along the length of the laminate. The lack of constraint along the width direction makes such a delamination more dangerous to the operation of the laminate, and at the same time simplifies the analytical solution of the problem.

4.2 Modelling approach

Consider a strip delamination of length 2*a* across the width *b* of a long isotropic composite laminate, as shown in Figure 4.1a. The delamination is located at a depth *h* below the surface in the laminate of thickness *t* (Figure 4.1b). The delamination can be regarded as a plane strain interface crack between the thin (*h*) and thick (*H*) parts of the laminate ($t = h + H$) and only a longitudinal section of unit width need be considered.

The unbuckled thin ply of the laminate is under a uniform in-plane compressive stress $\sigma_{xx} = -\sigma$. This stress will be defined below. Assuming that $h << a$, the thin ply can be regarded as a long, clamped Euler column of length 2*a*. It is further assumed that the

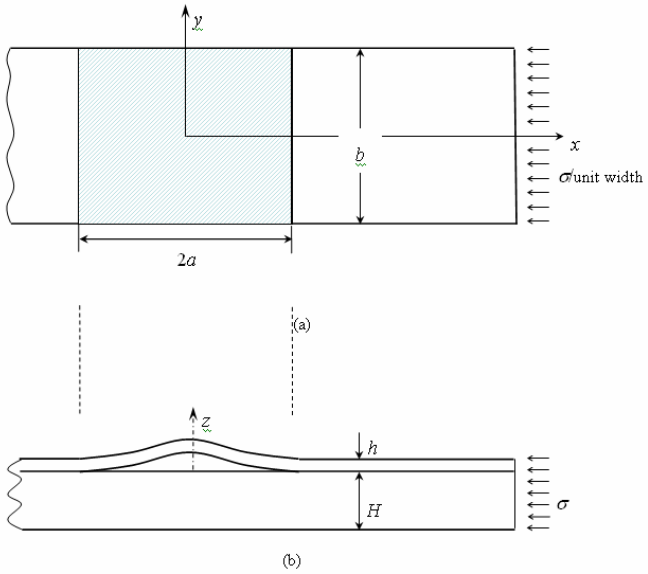

Figure 4.1. A strip delamination of length 2a in a long isotropic composite laminate of width b and thickness t = h + H before buckling (a) and after buckling (b).

underlying ply of thickness *H* is sufficiently stiff to offer a rigid support to the thin ply, i.e. $H >> h$. It is then possible to use the bi-layer solution of Hutchinson and Suo (1992) to characterize the interface crack tip field. But first let us consider the equilibrium of the laminate with interior strip delamination both before and after the it buckles (Figure 4.2). This will also help in defining the in-plane compressive stress. If the end of the laminate

is subjected to a compressive force P per unit width and a moment M_0 (also per unit width), then the forces in the thin and thick plies of the laminate before the delamination buckles are (Figure 4.2a)

$$F_1 = \frac{Ph}{h+H} + \frac{2M_0}{h+H} \quad F_2 = \frac{PH}{h+H} - \frac{2M_0}{h+H} \tag{4-1}$$

Denoting the compressive stress in the thin ply by σ, such that $F_1 = \sigma h$, gives for the assumed counter clockwise moment M_0

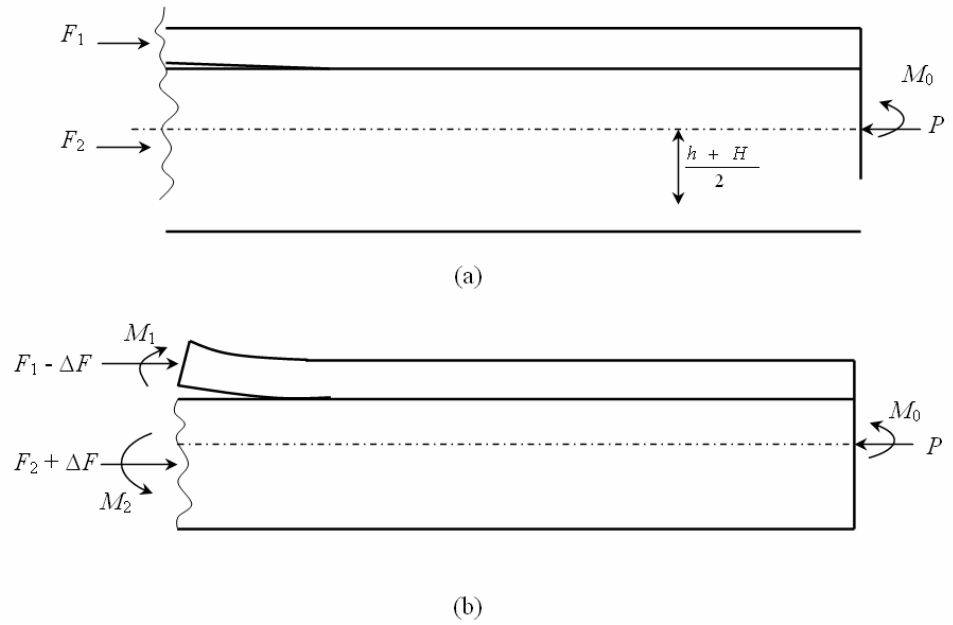

Figure 4.2. Equilibrium of the laminate before buckling of the strip delamination (a) and after buckling (b).

$$\sigma = \frac{P}{h+H} + \frac{2M_0}{h(h+H)} \equiv \frac{P}{t} + \frac{2M_0}{ht} \tag{4-2}$$

The sign of M_0 should be reversed in (4-2) if the applied moment is clockwise.

When the compressive stress σ on the thin ply of thickness h reaches the critical value σ_{cr} for a clamped-clamped Euler column of length $2a$ and flexural rigidity $D = Eh^3/[12(1-\nu^2)]$ per unit width, i.e.

$$\sigma_{cr} = \pi^2 D/\left(a^2 h\right), \tag{4-3}$$

it will buckle. This induces a moment M_1 and a change in the resultant axial compression ΔF near the tips of the interface crack (the right hand tip is shown in Figure 4.2b). These are calculated by considering the bending and stretching strains in the buckled thin ply measured from its unbuckled state using the von Karman non-linear plate theory (Hutchinson and Suo, 1992). The results are

$$\Delta F = \frac{3}{4} D \frac{\pi^2}{a^2} \xi^2$$

$$M_1 = \frac{\sigma_{cr}}{2}\xi h^2 \tag{4-4}$$

$$\xi \equiv \frac{w(0)}{h} = \left[\frac{4}{3}\left(\frac{\sigma}{\sigma_{cr}} - 1\right)\right]^{1/2}$$

Here, σ_{cr} is given by (4-3), ξ is the normalized maximum deflection of the buckled delamination, and σ is given by (4-2). From equilibrium requirements (Figure 4.2b),

$$M_2 = M_1 - \frac{\Delta F}{2}(h + H) \tag{4-5}$$

Before presenting expressions for the stress intensity factors at the right hand tip of the interface crack (Figure 4.2b) and for the energy release rate, it is worthwhile to comment on the origin of M_0. It can be construed to result from one of two sources. Firstly, it may be due to the fact that the line of action of the compressive force P does not coincide with the centroidal longitudinal axis of the laminate, in which case M_0 is simply the product of P and its eccentricity relative to the centroidal axis. This is quite likely to occur if long laminate specimens with deliberately introduced delaminations are tested under compression, as we shall see later. Secondly, it may be due to an initial curvature of the laminate. In this case, M_0 can be calculated from the initial (large) radius of curvature, R, and the bending stiffness of the laminate

$$M_0 = \frac{Et^3}{12(1-\nu^2)R}, \tag{4-6}$$

where $t = h + H$.

The energy release rate equals the difference of the strain energies per unit length per unit width stored in the edges far behind and far ahead of the crack tip, giving

$$G = \frac{1-\nu^2}{2E}\left[\frac{(F_1 - \Delta F)^2}{h} + 12\frac{M_1^2}{h^3} + \frac{(F_2 + \Delta F)^2}{H} + 12\frac{M_2^2}{H^3} - \frac{P^2}{h+H} - 12\frac{M_0^2}{(h+H)^3}\right]$$

which, after simplification, becomes

$$G = \frac{1-\nu^2}{2E}\left[\frac{(\Delta F)^2}{h} + \frac{(\Delta F)^2}{H} + 12\frac{M_1^2}{h^3} + 12\frac{M_2^2}{H^3} + \frac{4M_0^2(1-\eta+\eta^2)}{H^3\eta(1+\eta)^3} \mp \frac{4M_0}{H^2}\frac{\Delta F}{\eta}\right] \tag{4-7}$$

where $\eta = h/H \le 1$.

The above expression can also be obtained by using the J-integral formalism. An interface crack will begin to grow when the energy release rate (4-7) reaches a critical value, say $G_0(\psi)$, for the material. This value will however depend on the mode mixity parameter ψ defined by

$$\psi = \tan^{-1}\left(\frac{K_{II}}{K_I}\right), \tag{4-8}$$

where, K_I and K_{II} are the stress intensity factors which depends on η. Moreover, fibre-reinforced composite materials exhibit an *R*-curve behaviour, whereby the resistance of the material to crack growth increases as the crack advances until it reaches a steady state value. Sørensen *et al*. (2003) have proposed a DCB specimen loaded by unequal bending moments for constructing the complete *R*-curve and for back calculating the cohesive (bridging) force-crack opening and force-crack sliding laws responsible for the *R*-curve behaviour of these materials.

Substitution of (4-4) and (4-5) into (4-7) gives

$$G = \frac{1-\nu^2}{2E}\sigma_{cr}^2\left(\frac{\sigma}{\sigma_{cr}}-1\right)h\left[\frac{\sigma}{\sigma_{cr}}\left(1+4\eta+6\eta^2+3\eta^3\right)-\left\{48\left(\frac{\sigma}{\sigma_{cr}}-1\right)\right\}^{1/2}\eta^2\left(1+\eta\right)\right.$$
$$\left.+\left(3-4\eta-6\eta^2+\eta^3\right)\right] \qquad (4\text{-}9)$$
$$+\frac{4\left(1-\nu^2\right)}{2E}M_0\frac{\eta}{h}\left[\frac{M_0\eta}{h^2}\frac{1-\eta+\eta^2}{\left(1+\eta\right)^3}\mp\sigma_{cr}\left(\frac{\sigma}{\sigma_{cr}}-1\right)\right]$$

Note that the contribution of M_0 to G reduces rapidly as H increases. In the limit, when $\eta \rightarrow 0$, M_0 makes no contribution to G or to K_I and K_{II} (see equations (4-7) and (4-8)), and expression (4-9) reduces to that of Hutchinson and Suo (1992).

If a strip delamination is detected in a composite laminate during its manufacture or during a routine service inspection and its location and size ascertained, the above mathematical expressions can be used to assess the threat posed by it, as follows. Knowing the location (i.e. the depth of the delamination below the surface, h) and the size of the delamination ($2a$), the critical stress for its buckling σ_{cr} can be calculated from (4-3) and compared with the in-plane compression σ existing in the laminate along the longitudinal direction of the delamination. The situation of most concern to the manufacturer and/or the operator is $\sigma \geq \sigma_{cr}$ for the delamination will buckle away from the rest of the laminate. It is now necessary to know whether the delamination will start to grow in length as a result of buckling or simply keep bulging without extending. The transverse maximum deflection of the buckled delamination can be calculated from (4-4). It may be desirable to limit this deflection to prevent, for instance deterioration of the aerodynamic characteristics of the laminate. As far as the assessment of the buckling-driven growth of the delamination is concerned, expression (4-9), together with (4-4) and (4-5) is used to calculate the energy release rate G which is compared with the critical energy release rate $G_0(\psi)$ of the composite material. If the calculated energy release rate is equal to (or exceeds) the critical value $G_0(\psi)$ of the material, then the delamination will grow. How quickly and how far it will grow will depend on the *R*-curve behaviour of the laminate material, i.e. on the increase of $G_R(\psi)$ with crack growth.

The above procedure was verified by comparison with several test specimens tested in compression.

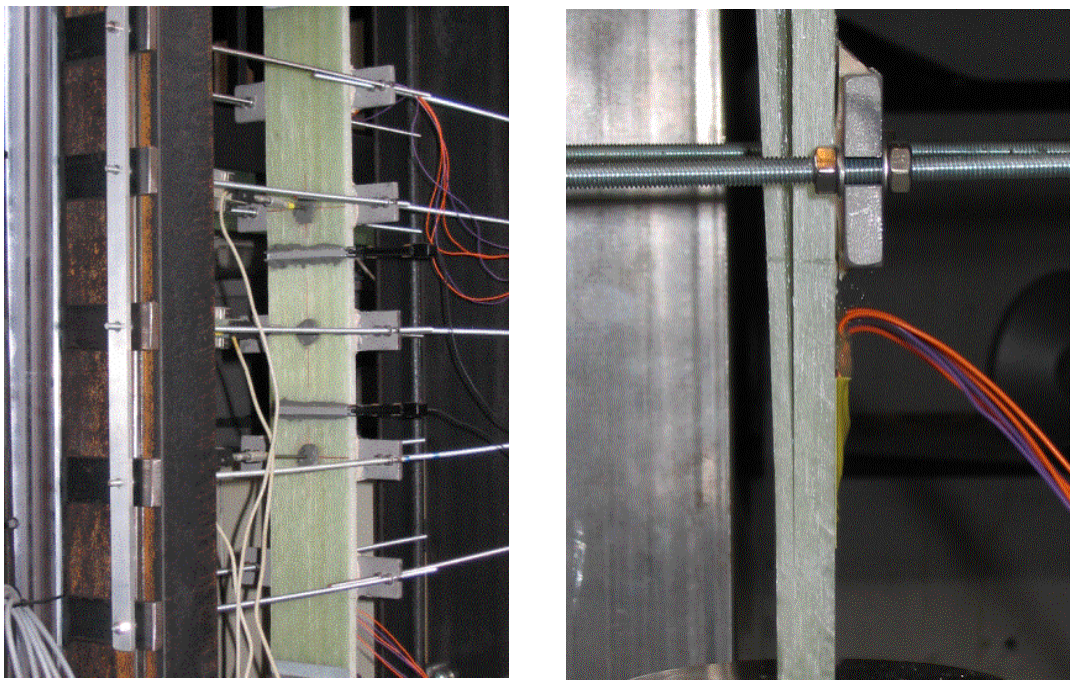

(a) (b)

Figure 4-3. Test setup. The picture to the left (a) shows the strip mounted in the testing machine. Shown is also the 5 intermediate supports allowing for vertical but not horizontal (transverse) movement. The picture to the left shows the crack tip at the delamination in the buckled state.

4.3 Tests

Seven specimens made from unidirectional glass fibre lamina were tested in the fibre direction under compression. Each specimen contained a delamination introduced with a thin Teflon sheet at the time of manufacture. The geometrical dimensions of the specimens and the length of the delamination were chosen to suit the capacity of the testing machine. The dimensions of two typical specimens are shown in Table 4-1. As the primary objective of these tests was to investigate the buckling-driven growth of the pre-existing delamination, the specimen was supported at several points in the lateral direction to increase its overall buckling load well beyond that needed to cause buckling of the delamination, as shown in Figure 4-3.

Table 4-1. Geometry of two typical test specimens (all dimensions in mm).

Test specimen	L	t	$2a$	h	b
1	800	13.25	152	4	100
5	800	12.78	254	4	100

The axial displacement of the specimen was continuously registered as the compressive load was increased. The transverse deflection of the specimens was measured with LVDTs located at the centre and the edges of the delamination giving the possibility of observing the buckling of the delamination and possible growth of the delamination.

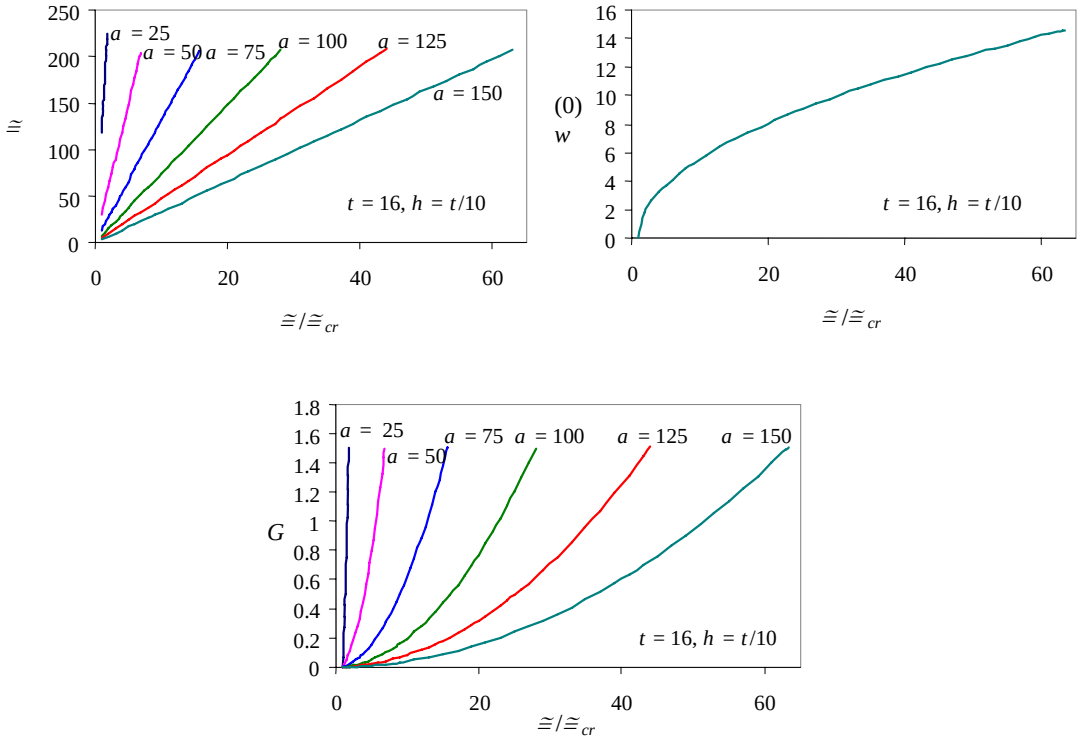

Figure 4-4. Graphs showing (a) design stress state, (b) maximum deflection and (c) energy release rate as functions of stress over critical stress for various lengths of the delamination. In all graphs t = 16 mm and h = t/10.

4.4 Conclusions

In the present work it was demonstrated that the post-buckling model can be used to assess whether a buckling-driven strip delamination in an isotropic composite laminate will grow in size or bulge in the transverse direction under an in-plane compressive stress. For the test specimens it was also possible to identify the source of discrepancy between the predicted and measured critical compressive stress at which the delamination buckled. In a practical situation it may not be possible to know whether there is any eccentricity. However, the source of a flexural contribution to the in-plane compressive stress may be the (large) curvature of the laminate in which a delamination has been detected. It is then easy to calculate the bending moment resulting from the curvature (4-6). The model can however be used irrespective of whether or not the source of M_0 can be identified. It is sufficient to know the net in-plane compressive stress in the composite laminate at the location of the detected delamination and the size of the delamination in order to assess the threat posed by it to the integrity of the laminate. Once the size ($2a$) and the location (h) of the delamination in a laminate have been ascertained, tables or graphs can be constructed to make the assessment according to the procedure outlined above. A few typical graphs for the variation of σ, $w(0)$ and G with σ/σ_{cr} for several values of h and t ($\eta = h/(t\text{-}h)$) are shown in Figures 4 (a)-(c). These figures can serve as a useful visual guide during design and inspection stages, if they are supplemented by lines corresponding to limits on design stress σ, and the maximum permissible deflection $w(0)$, and lines representing the critical energy release rates at the initiation of delamination growth $G_0(\psi)$ and during its propagation $G_R(\psi)$. The critical energy release rates will of course depend on the material and on how far the delamination has grown stably.

5 Adhesive joints

5.1 Introduction: Describing the failure process zone by cohesive laws

Cohesive laws, describing the mechanical stress-separation behaviour of a failure process zone, are widely used in models of problems involving crack initiation and growth. However, methods for determination of cohesive laws are not well established. Here, a J integral approach was developed for determining mixed mode cohesive laws.

The situation to be analysed is shown in Fig. 5.1. The problem is a two-dimensional crack-bridging problem lying in the x_1-x_2-plane. The crack is parallel to the x_1-axis. The failure process zone is divided into two parts: the crack tip, where a singular stress field exist, and a bridging zone in the crack wake. The present approach is not limited to a small-scale bridging zone. However, small displacements and small strains are assumed.

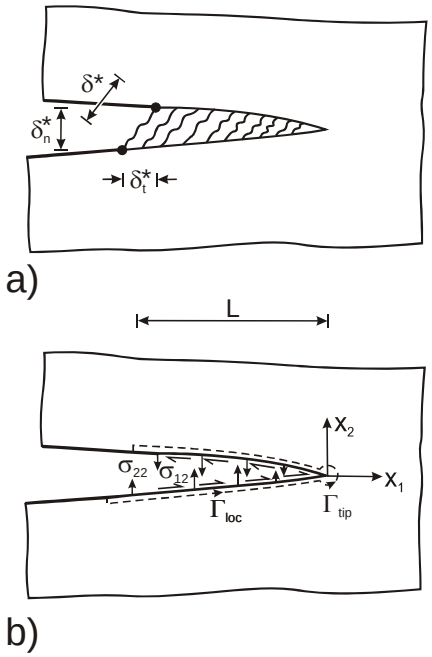

Figure 5.1: A crack, experiencing large-scale bridging, subjected to mixed mode crack opening displacement.

It is furthermore assumed that the crack opens in a monotonic fashion. Then, it is reasonable to assume that within the bridging zone the local cohesive stresses is a function only of the local normal and tangential crack opening displacements

$$\sigma_{22} = \sigma_{22}\left(\delta_n, \delta_t\right) \quad \sigma_{12} = \sigma_{12}\left(\delta_n, \delta_t\right), \tag{5-1}$$

where σ_{22} is the normal stress and σ_{12} is the shear stress transmitted across the crack faces within the bridging zone. The relationships (2) are the *mixed mode cohesive laws*. The cohesive laws are assumed to be the same for each point along the cohesive zone. They are thus considered as material properties, i.e., and independent of specimen geometry. Since the cohesive stresses represent the failure process zone, it is reasonable to assume that for some crack opening, the failure process zone has failed completely, so that the cohesive stresses vanish.

5.2 J integral approach for cohesive law determination

Evaluating the path independent J integral along we obtain

$$J_{loc} = \int_0^{\delta_t^*} \sigma_{12}(\delta_n, \delta_t)\, d\delta_t + \int_0^{\delta_n^*} \sigma_{22}(\delta_n, \delta_t)\, d\delta_n + J_{tip}\,, \tag{5-2}$$

where δ_n^* and δ_t^* are the end-opening and end-sliding of the cohesive zone. Finally, we assume that the stresses are derived from a displacement potential, Φ

$$\sigma_{22}(\delta_n, \delta_t) = \frac{\partial \Phi(\delta_n, \delta_t)}{\partial \delta_n} \qquad \sigma_{12}(\delta_n, \delta_t) = \frac{\partial \Phi(\delta_n, \delta_t)}{\partial \delta_t}. \tag{5-3}$$

Inserting (5-3) into (5-2), we obtain

$$J_{loc} = \Phi(\delta_n^*, \delta_t^*) + J_{tip}\,. \tag{5-4}$$

Crack propagation occurs when J_{tip} is identical to the fracture energy of the crack tip, J_0, which is assumed to be a material constant. During crack growth, the value of J_{loc} is denoted J_R, the fracture resistance of the material,

$$J_R = \Phi(\delta_n^*, \delta_t^*) + J_0\,. \tag{5-5}$$

The energy uptake by the crack tip is assumed to be constant under cracking. Then, J_R increases with increasing crack length, since δ_n^* and δ_t^* increase during cracking. The fracture resistance is assumed to reach a steady-state value, J_{ss}, when the bridging zone is fully developed, and the crack opening at the end of the bridging zone is so large that the cohesive stresses are zero there. Combining (5-3) and (5-5) we obtain

$$\sigma_{22}(\delta_n^*, \delta_t^*) = \frac{\partial J_R(\delta_n^*, \delta_t^*)}{\partial \delta_n^*} \qquad \sigma_{12}(\delta_n^*, \delta_t^*) = \frac{\partial J_R(\delta_n^*, \delta_t^*)}{\partial \delta_t^*}\,, \tag{5-6}$$

since J_0 is assumed to be constant during cracking. It follows from (5-6) that mixed mode cohesive laws can be derived by simultaneous measurements of J_R, δ_n^* and δ_t^*. That is the key idea of the approach.

In practice, a surface fit is made to the J_R-δ_n^*-δ_t^* data after a suitable normalisation of δ_n^* and δ_t^*, denoted $\bar{x}$ and $\bar{y}$, respectively. Fitting was done with a double Chebyshev series of the form

$$f(\bar{x}, \bar{y}) = \sum_{i=0}^{k} \sum_{j=0}^{l} a_{ij} T_i(\bar{x}) T_j(\bar{y})\,, \tag{5-7}$$

where $T_i(\bar{x})$ and $T_j(\bar{y})$ are the Chebyshev polynomial of the first kind of degree i and j, respectively, and k and l denote the maximum polynomial degree of $T_i(\bar{x})$ and $T_j(\bar{y})$. Afterwards, approximate functions for the cohesive law were obtained by differentiation.

5.3 Test of approach with synthetic data

In order to test the feasibility of the proposed approach, we test it by synthetic data. Here, only a few examples are given. A more comprehensive investigation is given in the paper (Sørensen and Kirkegaard, 2005). Since the synthetic data should mimic experimental data, the starting point of the approach is the J_R- δ_n^* - δ_t^* data. Without loss of generality, the crack tip fracture energy, J_0 is set to zero (J_0 is assumed to be constant under crack growth and thus vanishes under the differentiation). For the purpose of the investigation we have selected an axisymmetric power law function, given by

$$\frac{J_R(\delta^*)}{J_{ss}} = \frac{\left(\delta^*/\delta_0 + \xi\right)^n - \xi^n}{\left(1+\xi\right)^n - \xi^n} \tag{5-8}$$

as our basic cohesive law. In (5-8), δ_0 is the end-opening at which J_R reaches J_{ss} and the cohesive stress vanish, ξ and n are dimensionless parameters that control the shape of the J_R curve. Examples of J_R-δ^* curves are given in Fig. 5.2.

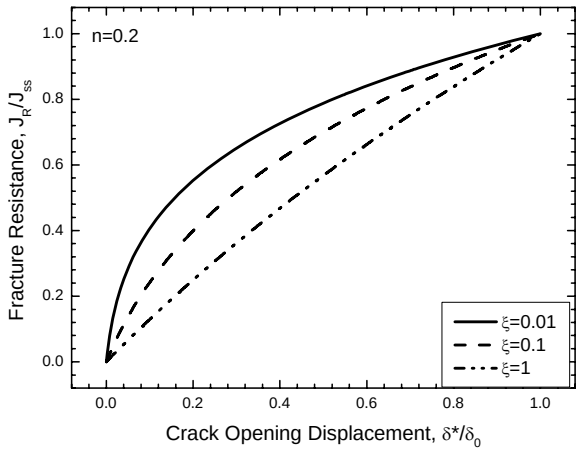

Figure 5.2: Examples of model J_R-δ curves.*

Datasets of J_R a function of δ_n^* and δ_t^* were generated from (5-8) for various phase angles, with a fixed angle, $\Delta\varphi$, between each dataset. Since the aim is to obtaining σ_{22} and σ_{12} as accurate as possible, we compare σ_{22} and σ_{12} with the values obtained by the analytical solution. For pure normal opening (δ_t^* = 0) the normal stress becomes

$$\sigma_{22}(\delta_n, \delta_t = 0) = \frac{J_{ss}}{\delta_0} \frac{n\left(\delta_n/\delta_0 + \xi\right)^{n-1}}{\left(1-\xi\right)^n - \xi^n} \quad . \tag{5-9}$$

Fig. 5-3 shows $\sigma_{22}(\delta_n, \delta_t = 0)$ obtained from the J_R-data for fits using different values of $k = l$. The analytical solution (11) is also shown for comparison. It is seen, that for the parameter chosen, the shape is recovered reasonably well for $k = l \geq 3$. However, in order to obtain a peak stress, $\hat{\sigma}_{22}$, within 10 % of the analytical value, $k = l$ must be 6 or larger.

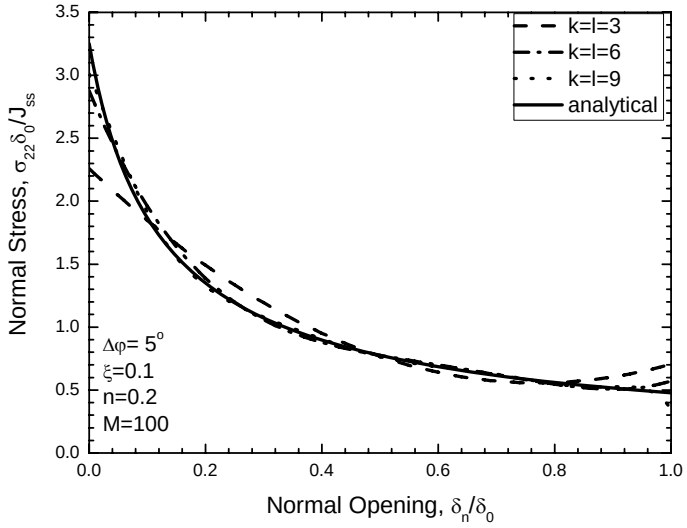

Figure 5.3: The normal cohesive stress, σ_{22}, as a function of pure normal opening, δ_n, determined for various values of the maximum polynomial degree (k = l).

The effect of the noise parameter, ω, on the J_R-δ^* data is illustrated in Fig. 5-4. The noise variation associated with ω = 0.05 is very large; the noise corresponding to ω = 0.01 is probably most realistic while ω = 0.005 represents data with very low noise.

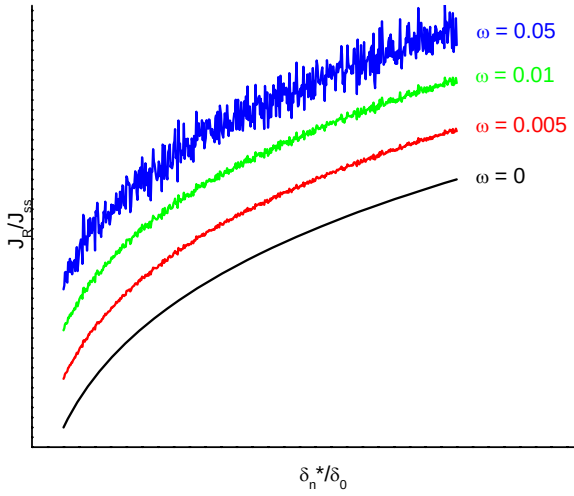

Figure 5.4: Synthetic R-curve data (J_R as a function of end-opening, δ_n^*) with various noise levels.

Fig. 5-5 shows σ_{22} as a function of δ_n (i.e., with δ_t = 0) obtained from data with different noise levels. For ω = 0.005 the cohesive stress is very similar to that obtained by the use of the noiseless data (Fig. 8). For ω = 0.01 the results is still reasonably good; the shape is established rather well but the peak stress is significantly below the correct value. For ω = 0.05 neither the peak stress nor the cohesive law shape are determined well.

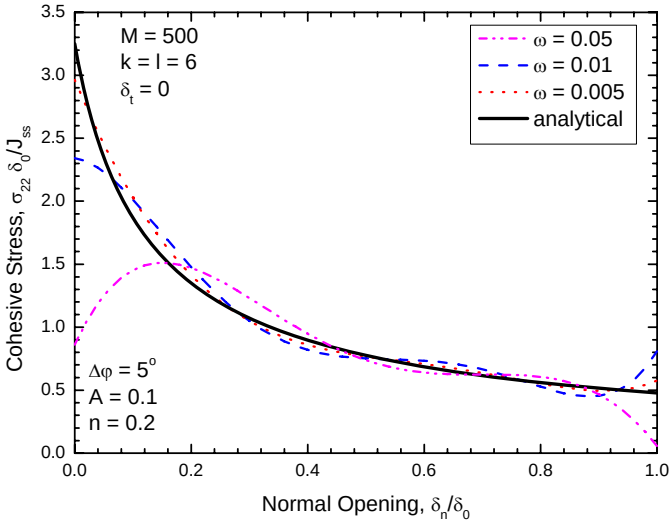

Figure 5.5: The normal cohesive stress, σ_{22}, as a function of pure normal opening, δ_n, determined from synthetic data with various values of the noise level, ω.

5.4 Conclusions

In conclusion, a novel approach for the determination of mixed mode cohesive laws has been proposed. Its capability to determine cohesive laws has been investigated by synthetic data. The approach seems feasible. Mixed mode cohesive laws can be determined accurately if the following requirements are fulfilled (Sørensen and Kirkegaard, 2005):

- the number of different datasets (different loading conditions) should be six or more,
- the number of data points per dataset should be at least 500,
- the polynomial degree to fit to the J_R-data, $k = l$, should be 3 or higher to provide a reasonably accurate cohesive law shape,
- determination of the peak cohesive stress requires a polynomial degree, $k = l$, of 6th order or higher,
- the peak stress can be determined accurately by using only the steepest part of the data, e.g., $0 \le \delta^*/\delta_0 \le 0.1$, and
- the standard deviation of the noise in the data, ω, should be less than 0.01 times the maximum value of the fracture resistance and the end-opening and end-sliding.

6 Delamination of unidirectional fibre composites

6.1 Introduction

Layered structures can fail along weak interfaces. Examples are failure of adhesive joints, sandwich structures and delamination of laminates made of fibre composites. Delamination of fibre composites is often accompanied by fibre bridging. Fibre bridging results in increasing fracture resistance. The purpose here is to characterise the fibre bridging in terms of cohesive laws, using the approach developed for adhesive joints (section 5). The cohesive laws were thus derived from fracture mechanics testing of

Double cantilever beam specimens loaded with uneven bending moments (DCB-UBM). Here, only a brief summary will be give. Full details will be published elsewhere (Sørensen and Jacobsen, 2005).

6.2 Experimental methods

DCB specimens were made from a unidirectional fibre composite made by vacuum infusion. Steel parts were bonded to the ends to allow gripping. The specimens were tested in a special loading fixture that allows uneven bending moments for each DCB arm. By varying the ratio between the moments, the end-openings of the cohesive zone can be varied from normal opening to pure tangential crack opening displacement.

The normal- and tangential directions of the end-opening of the cohesive zone, δ_n^* and δ_t^*, are calculated from measurements of the displacements of the mid-planes of the beams, Δ^E, as well as two displacements parallel with one of the beams, Δ_1^L and Δ_2^L, see Fig. 6.1.

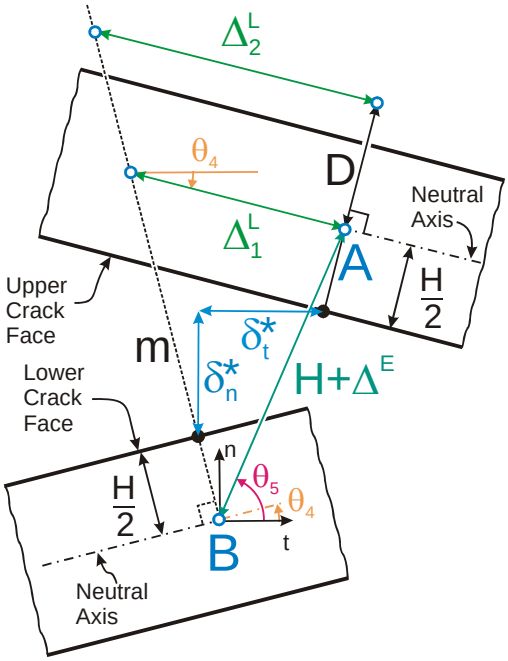

Figure 6.1: Geometry of determination of normal and tangential end-openings from measurements of Δ^E, Δ_1^L and Δ_2^L.

By the use of trigonometry, the normal- and tangential directions of the end-opening of the cohesive zone are obtained as

$$\delta_n^* = \left(H + \Delta^E\right)\sin\theta_5 - H\cos\theta_4 \quad \text{and} \quad \delta_t^* = \left(H + \Delta^E\right)\cos\theta_5 \,, \tag{6-1}$$

where H denote the beam height, and

$$\theta_4 = \tfrac{1}{2}\tan^{-1}\left(\frac{\Delta_2^L - \Delta_1^L}{D}\right), \tag{6-2}$$

with D being the distance between the two measurements axis (see Fig. 6.1) and (measuring angles in radians)

$$\theta_5 = \theta_4 + \frac{\pi}{2} - \sin^{-1}\left\{\frac{\Delta_1^L}{H + \Delta^E}\cos(2\theta_4)\right\}. \qquad (6\text{-}3)$$

The procedure for data analysis is shown in Fig. 6.2. Following experiments conducted with various different rations of moments, the fracture resistance and end openings are calculated. Next a function consisting of a double Chebyshev series is fitted to the J_R-δ_n^*-δ_t^* data from all experiments. Approximate functions for the cohesive stresses are then obtained by partial differentiation.

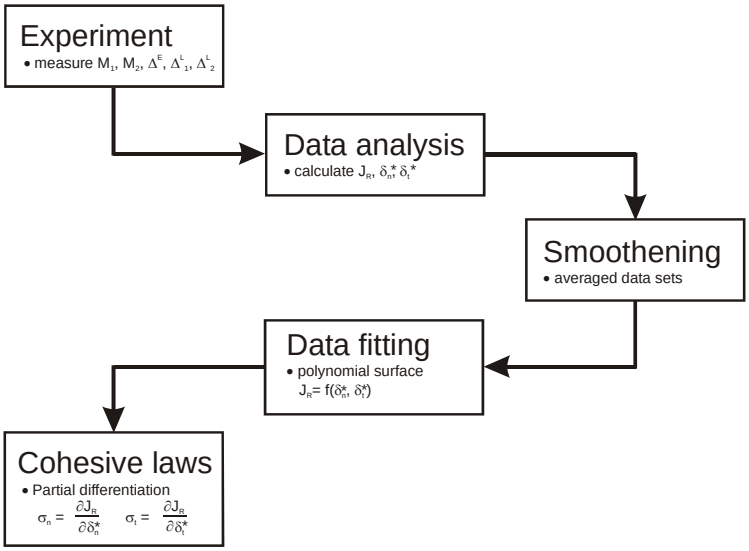

Figure 6.2: Procedure for obtaining cohesive law from fracture mechanics experiments.

6.3 Experimental results

Examples of measured J_R-δ_n^*-δ_t^* data is shown in Fig. 6.3. In Fig. 6.3, the data are normalised by their maximum values. Note, that the fracture resistance of experiments dominated by tangential end-openings rises to a significant higher steady-state level than for experiments with dominating normal end-openings.

Results, cohesive stresses as a function of δ_n^* and δ_t^* are shown in normalised form in Fig. 6.4 and Fig. 6.5. The results were obtained by fitting a fourth order Chebyshev polynomials to the measured J_R-δ_n^*-δ_t^* data followed by partial differentiation. The cohesive stresses are set to zero in the steady-state region. Three things are obvious from the results. First, the cohesive stresses start at the peak value and decrease with increasing crack opening. Second, the normal and shear stress depend both on the normal and tangential crack opening displacements. Third, the peak shear stress is more than seven times as high as the peak normal stress.

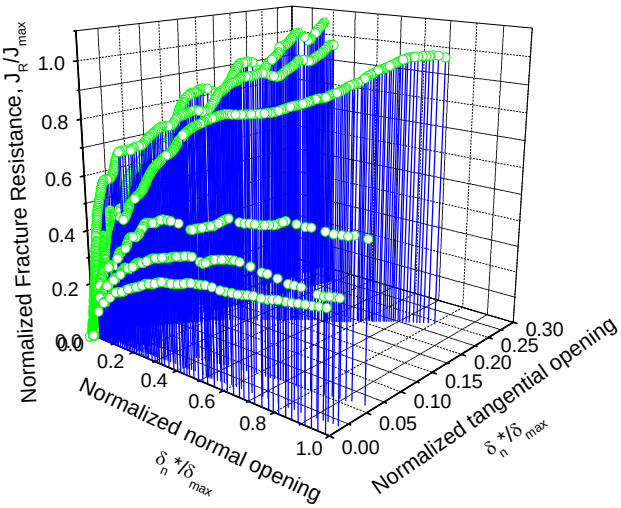

Figure 6.3: Measured (normalised) fracture resistance as a function of normalised normal and tangential end-openings.

6.4 Conclusions

The problem of characterising delamination fracture resistance was addressed by cohesive laws. The cohesive stresses were successfully obtained by the use of the novel approach based on the J integral (section 5). The determined cohesive laws can be used in models of composite structures experiencing delamination.

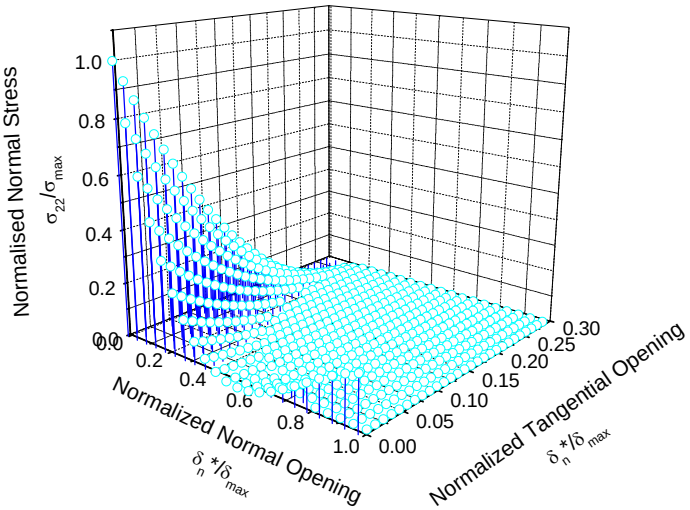

Figure 6.4: Cohesive normal stress (normalised by the peak normal stress) as a function of normalised normal and tangential crack opening displacements.

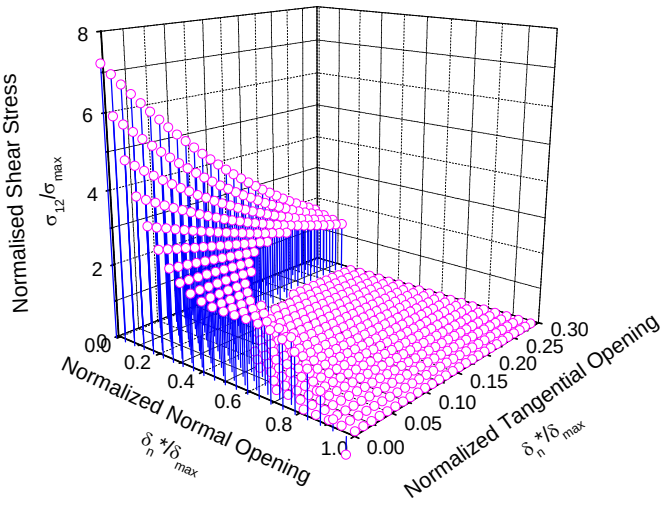

Figure 6.5: Cohesive shear stress (normalised by the peak normal stress) as a function of normalised normal and tangential crack opening displacements.

7 Simulation of gelcoat delamination at a corner

7.1 Introduction

Spontaneous delamination of thin layers and initiation of interface cracking in bonds may occur at sufficiently large flaws at the interface. It may also occur at corners and edges due to the stress concentrations there. A large effort is currently spent in characterising interface fracture at corners and edges (see e.g. Borgesen *et al.*, 2000; Begley and Ambrico, 2001; and Ayhan and Nied, 2001).

The basic geometry considered in the present work is sketched in Fig. 1: A thin layer bonded to a substrate contains an interface crack of length L close to a corner with the opening angle γ. The stress state in the bonded layer is homogeneous and equi-biaxial. The objective is to determine the shape of the crack front, C, and to determine the conditions for which such interface cracks may exist.

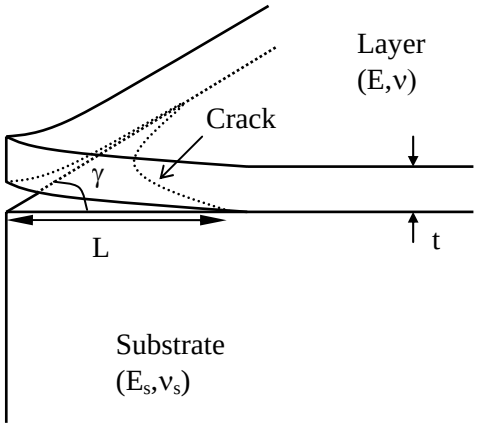

Figure 7.1: Geometry analysed: An interface crack between a thin layer and a substrate is located close to a corner.

7.2 Interface fracture

In the analysis the following fracture criterion is assumed (Jensen, Hutchinson and Kim, 1990)

$$\left(\frac{1-\nu^2}{E}+\frac{1-\nu_s^2}{E_s}\right)\frac{K_1^2+\lambda_2 K_2^2}{2} + \left(\frac{1}{\mu}+\frac{1}{\mu_s}\right)\frac{\lambda_3 K_3^2}{4} = G_{1c} \tag{7-1}$$

where E, ν and μ are the Young's modulus, Poisson's ratio and the elastic shear modulus of the layer while subscript $(\,)_s$ refers to properties of the substrate. In (7-1) K_1 , K_2 and K_3 are the mode 1, 2 and 3 stress intensity factors for the interface crack front, C, which in the general case vary along the front. Furthermore, in (1) λ_2 and λ_3 are factors between 0 and 1 adjusting the relative contribution of modes 2 and 3 to the fracture criterion, and G_{1c} is the mode 1 interface fracture toughness.

Under the assumptions mentioned above, (7-1) reduces to

$$\sigma_{nn}^2+\frac{\lambda}{1-\nu}\sigma_{nt}^2 = \sigma_c^2 = \frac{2EG_c^*}{(1-\nu^2)t} \tag{7-2}$$

where

$$\lambda = \frac{\lambda_3}{1+(\lambda_2-1)\sin^2\psi}$$
$$G_c^* = \frac{G_{1c}}{1+(\lambda_2-1)\sin^2\psi} \tag{7-3}$$

Here, the properties of the substrate affect the fracture criterion through $\psi = \psi(\alpha,\beta)$ where the Dundurs' parameters are denoted α and β. In the case that the second Dundurs' parameter β is zero, the phase angle of loading ψ is given by

$$\tan\psi = \frac{K_2}{K_1} \tag{7-4}$$

Finally, in (7-2) σ_{nn} and σ_{nt} are the differences in the values of normal and shear stress across the crack front. These stresses are for most of the results presented below calculated by the finite element method.

The stress state in the bonded layer is assumed to be equi-biaxial. The stresses in the delaminated part of the layer are inhomogeneous and partly relieved due to the presence of the stress free edges. The material behaviour is assumed to be linear elastic, however, the problem is non-linear due to the shape of the crack front being unknown. As a result the solution is found numerically by an iterative procedure as described in the following.

The stress σ_c in (7-2) can be interpreted as the critical stress required to propagate a straight-sided edge crack under plane strain conditions. Thus, crack propagation is not possible unless the stress exceeds σ_c. Close to a corner, however, there is a stress concentration, and crack propagation at lower stress levels is possible.

7.3 Corner delamination

As illustrated in Fig. 7.2 the solution to the problem is divided into two sub problems. The first of these is trivial while the other is solved by the finite element method assuming plane stress conditions in the delaminated layer.

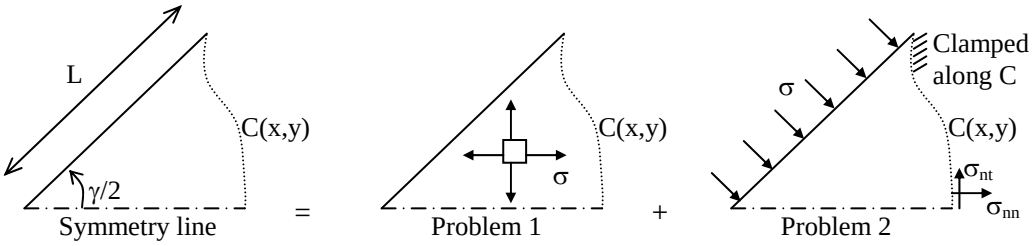

Figure 7.2: The problem is divided into sub problems 1 and 2. The finite element method is used for calculating σ_{nn} and σ_{nt} for sub problem 2.

For a given shape of the crack front, a given stress level and a given interface fracture criterion the stresses σ_{nn} and σ_{nt} are calculated. In general (7-2) will not be satisfied so the shape is adjusted iteratively in order to minimise ε defined as

$$\varepsilon = \sum_{i=1}^{N} W_i G_i^2 \tag{7-5}$$

where N is the number of finite elements along the crack front. The weighting functions W_i in (7-5) are chosen to be equal to 1, and the object functions G_i are defined as

$$G_i = \sigma_c^2 - \sigma_{nni}^2 - \frac{\lambda}{1-\nu}\sigma_{nti}^2 \tag{7-6}$$

The unknowns in (7-5) are the co-ordinates of the nodal points in the finite element mesh which are located at the crack front. These unknowns are determined by minimisation of ε which is performed by Newton-Raphson iteration (see Pane and Jensen, 2005). The derivatives of ε with respect to the nodal co-ordinates are found numerically. The iterations are terminated when the root mean square gets below a specified value. In most of the cases in the following the specified error is 1%. In each of the iterations, the entire finite element mesh is updated.

7.4 Numerical results

Some numerical results for the shape of the crack front at steady-state delamination are shown below. In Fig. 7.3 results for the shape of the crack front for different values of λ are shown for a residual stress $\sigma/\sigma_c = 0.8$ which is smaller than the stress required to propagate the crack under plane strain conditions. As seen by Fig. 7.3 the parameter λ which characterises the interface fracture criterion has a significant effect on the shape of the delaminated region.

It is also obvious by Fig. 7.3 that steady state delamination at a corner is possible at lower stress levels than the design stress $\sigma = \sigma_c$. It is for this reason of interest to examine the range of stress levels for which corner delaminations are possible, which is the purpose of the following Section.

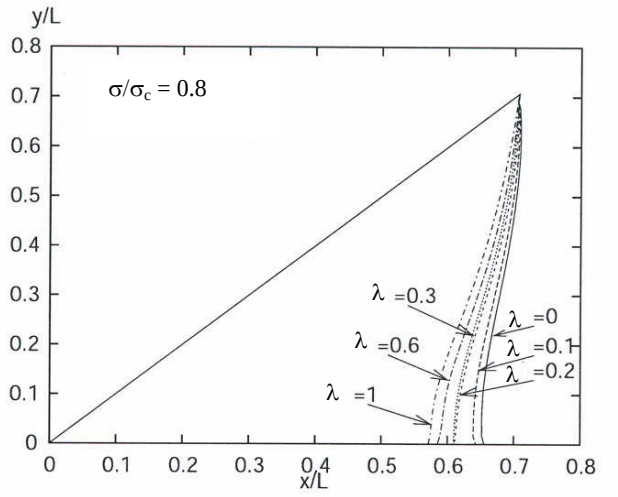

Figure 7.3: Shape of crack front at steady-state delamination for different fracture criteria at low stress levels.

7.5 Conditions for steady-state delamination

The intersection point between the crack front and the free edge is analysed on a scale which is small compared to the crack length, L, but still large compared to the layer thickness, h. The geometry for sub problem 2 in Fig. 7.2 on this scale is shown in Fig. 7.4. The angle of intersection is denoted ω. A closed form solution can be obtained for this problem and is given by

$$\sigma_{nn} = -\frac{2\sigma\cos 2\omega}{1-\nu+(1+\nu)\cos 2\omega}$$
$$\sigma_{nt} = -\frac{(1-\nu)\sigma\sin 2\omega}{1-\nu+(1+\nu)\cos 2\omega} \qquad (7\text{-}7)$$

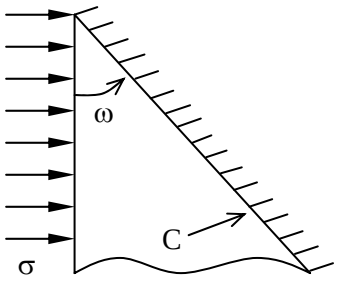

Figure 7.4: Geometry for local analysis at point of intersection between crack front and stress free edge.

Inserting these stresses in the fracture criterion (7-2) results in the following relationship between the residual stress in the layer, σ, the angle of intersection, ω, and the parameter λ entering the fracture criterion

$$\frac{\sigma}{\sigma_c} = \frac{1-\nu+(1+\nu)\cos 2\omega}{\sqrt{4\cos^2 2\omega+\lambda(1-\nu)\sin^2 2\omega}} \qquad (7\text{-}8)$$

A plot of this relationship for ν = 1/3 is shown in Fig. 5. When the denominator in (7-7) becomes zero, singular stresses exist at the intersection point between the crack front and

the stress free edge. This angle is $\omega = 60^o$ for $\nu = 1/3$. For angles greater than or equal to 60^o singular stresses exist and as a result the fracture criterion (2) always is exceeded and steady state delamination is impossible. At the minimum stress indicated in Fig. 5 steady-state delamination is possible with $\omega = 60^o$. As the residual stress is further increased, the angle of intersection between the crack front and the stress free edge decreases until the point of maximum stress in Fig. 7.5 is reached. By Fig. 7.5 it is seen that this maximum stress is close to 45^o for values of λ less than 1. For values of λ greater than or equal to 1 the maximum stress is $\sigma/\sigma_c = 1$ at $\omega = 0^o$. If the residual stress is increased beyond the maximum in Fig. 7.5, steady-state delamination at the corner is not possible. It should be noted that propagation of a straight-sided edge crack is always possible for $\sigma/\sigma_c > 1$ and for that reason the most interesting range of residual stresses for the propagation of a corner crack is $\sigma/\sigma_c < 1$. If, for example, $\lambda = 0.1$, then by Fig. 7.5 steady-state delamination at the corner is not possible for $\sigma/\sigma_c < 0.5$. This minimum value of the critical residual stress may in addition to σ_c be important for the design of layered systems.

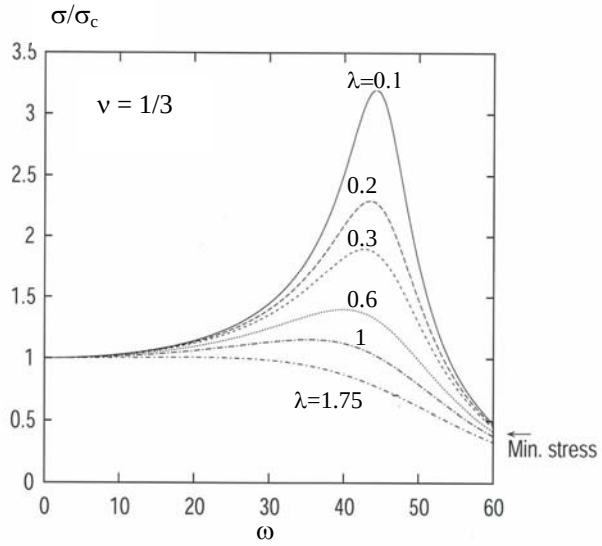

Figure 7.5: Normalised stress versus angle of intersection between crack front and stress free edge ($\gamma = 45^o$).

7.6 Conclusion

Steady-state delamination of a thin layer on an elastic substrate close to corners and edges were analysed. A local analysis of the region close to the intersection point between the crack front and the free edge showed that steady-state delamination at corners is possible at stress levels lower than those required to make an edge crack propagate under plane strain conditions due to the stress concentrations at interface corners.

A numerical method based on the finite element method coupled to exact solutions near to the crack tip for calculating the shape of the crack front was outlined. The method involves an iterative procedure to adjust the shape of the crack front so that the fracture criterion is satisfied locally along the front. Results based on the numerical scheme demonstrated the sensitivity of the crack front shape to the interface fracture criterion and the level of residual stresses.

8 Conclusions

The wind turbine blade tested to failure in Phase I was modelled by finite element analysis. The analysis shows that when the blade buckles locally in the downwind side, the strains are so high that they lead to progressive failure of the blade.

The deformation of a section of a box girder, subjected to transverse forces, was measured experimentally. A very good agreement was found between the measured displacements and those predicted by a finite element model and a beam model with springs at the ends.

A J integral method was developed for the determination of mixed mode cohesive laws from crack growth experiments. Requirements for the "quality" of data were determined by the use of synthetic data.

Delamination of a thin layer at a corner was analysed. The results show that delamination at the corner is possible at lower residual stresses that required for steady state propagation of an edge crack.

9 List of publications from the current project

Jacobsen, T. K., and Sørensen, B. F., 2005, "Strength scaling mechanics of polymer composites", *Composites*, manuscript in progress.

Karihaloo, B. L. and Stang, H., 2005, "Buckling-driven delamination growth in composite laminated: guidelines for assessing the threat posed by a delamination", submitted for publication.

Karihaloo, B. L. and Stang, H., 2005, "Buckling-driven delamination growth in composite laminated: guidelines for assessing the threat posed by a delamination", Report, BYG.DTU.

Kühlmeier, L.; Halling, K. M.; Lund, E.; Thomsen, O. T. (2004): ``Buckling Analysis of Generally Laminated Cylindrical Shells - An Analytical Approach". In: Proc. 17th Nordic Seminar on Computational Mechanics, (Eds. A. Eriksson, J. Månsson, G. Tibert), Stockholm, 2004, pp. 54-57.

Lund, E.; Kühlmeier, L.; Stegmann, J. (2005): ``Buckling Optimization of Laminated Hybrid Composite Shell Structures Using Discrete Material Optimization". In: *Proc. WCSMO6 - 6th World Congress on Structural and Multidisciplinary Optimization*, 30 May - 3 June 2005, Rio de Janeiro, Brazil, CD-ROM, 10 pages.

Lund, E.; Stegmann, J. (2004): ``On Structural Optimization of Composite Shell Structures Using a Discrete Constitutive Parameterization". In: *The Science of making Torque from Wind*, (ed. G.A.M. van Kuik), 19-21 April 2004, DUWind, Delft University of Technology, ISBN 90-76468-10-9, pp. 556-567.

Lund, E.; Stegmann, J. (2005): ``On Structural Optimization of Composite Shell Structures Using a Discrete Constitutive Parameterization". *Wind Energy*, Vol. 8, Issue 1, pp. 109-124.

Lund, E.; Stegmann, J. (2005): ``Eigenfrequency Optimization of General Composite Shell Structures Using a Discrete Material Optimization Approach". In: *Proc. 12th International Congress on Sound and Vibration*, 11 - 14 July, Lisbon, Portugal, CD-ROM, 8 pages.

Overgaard, L. (2004): “On Structural Assessment of Failure Mechanisms and Instability Phenomena in the V52 Wind Turbine Blade Static Test Performed within the EFP2003 Programme”. *Preliminary test report.*

Overgaard, L.; Lund, E. (2005A): “Structural Design Sensitivity Analysis and Optimization of Vestas V52 Wind Turbine Blade”. In: *Proc. 6th World Congress*

on Structural and Multidisciplinary Optimization, 30 May - 3 June, Rio de Janeiro, Brazil, CD-ROM, 10 pages.
Overgaard, L.; Lund, E. (2005B): “Static Test to Structural Collapse of a V52 Wind Turbine Blade, Part A: Assessment of Structural Collapse”. in progress.
Overgaard, L.; Lund, E. (2005C): “Static Test to Structural Collapse of a V52 Wind Turbine Blade, Part B: Synthesis between Blade Response and Predictive Models”. in progress.
Pane, I., and Jensen, H. M., "Steady-state delamination of thin films at corners" (in preparation).
Pardo D.R. & Branner K. (2005) “Finite Element Analysis of the Cross-section of Wind Turbine Blades; A Comparison between Shell and 2D-Solid Models”, Wind Engineering, Volume 29, No. 1, 2005.
Stegmann, J.; Lund, E. (2005): ``Discrete Material Optimization of General Composite Shell Structures". *International Journal for Numerical Methods in Engineering*, Vol. 62, No. 14, pp. 2009-2027.
Stegmann, J.; Lund, E. (2005): ``Discrete Material Optimization of Laminated Composite Shell Structures Using Local Strain Criteria". In: *Proc. WCSMO6 - 6th World Congress on Structural and Multidisciplinary Optimization*, 30 May - 3 June 2005, Rio de Janeiro, Brazil, CD-ROM, 10 pages.
Stegmann, J.; Lund, E. (2005): Nonlinear Topology Optimization of Layered Shell Structures. *Structural and Multidisciplinary Optimization*, Vol. 29, pp. 349-360. Sørensen, B. F., and Jacobsen, T. K., 2005, "Delamination of fibre composites: determination of mixed mode cohesive laws", *Journal of the Mechanics and Physics of Solids*) manuscript in progress.
Sørensen, B. F., and Kirkegaard, P., 2005, "Determination of mixed mode cohesive laws", *Engineering Fracture Mechanics*, manuscript in progress.
Sørensen, B. F., Jørgensen, K., Jacobsen, T. K., and Østergaard, R. C., 2005, "DCB-specimen loaded with uneven bending moments", *International Journal of Fracture*, manuscript in progress.
Østergaard, R. C, and Sørensen, B. F., 2005, "Measurement of interface fracture toughness of sandwich structures", *Sandwich Structures 7: Advancing with Sandwich Structures and Materials* (eds. O.T.Thomsen, E. Bozhevolnaya and A. Lyckegaard), Springer, pp. 413-422.

In addition, parts of the activities in the project were described in popular form in the following articles:

"Nye fremskridt inden for afprøvning af designdetaljer", *LM Newsletter*, Februar 2005, p. 3.
"Klog af skade på vindmøllevinger", *Risø Nyt*, 1, 2003, pp. 44-45.

10 Other publications

Ayhan, A. O., and Nied, H. F., 2001, "Analysis of three-dimensional interface cracking in electronic packages", *Proc. Int. Conf. Fracture, ICF10 Honolulu, 2001, Pergamon Press* (on cd).
Begley, M. R., and Ambrico, J. M., 2001 "Delamination of thin films from two-dimensional interface flaws at corners and edges", *Int. J. Fracture*, vol. 112, pp. 205-222, 2001.
Borgesen, P., Blass, D. and Shrihari, K., 2000, "Flip chip reliability", *Proc. of IPC-APEX*, March 2000.
Hutchinson, J. W. and Suo, Z., 1992, "Mixed mode cracking in layered materials", In *Advances in Applied Mechanics*, 29 (eds. J W Hutchinson & T Y Wu), Academic Press, London, 63-191.

Jensen, H. M., Hutchinson, J. W., and Kim, K.-S., 1990, "Decohesion of a cut prestressed film on a substrate", *Int. J. Solids Structures*, vol. 26, pp. 1099-1114, 1990.

Sørensen, B. F., Jørgensen, E., Debel, C. P., Jensen, F. M., Jensen, H. M., Jacobsen, T. K., and Halling, K., 2004, "Improved design of large wind turbine blade of fibre composites based on studies of scale effects (Phase 1). Summary report". Riso-R-1390(EN), 36 p.

Sørensen, B. F., Jørgensen, K., Jacobsen, T. K. and Østergaard, R. C., 2003, "A general mixed mode fracture mechanics test specimen: The DCB-specimen loaded with uneven bending moments", *Report Risø – R – 1394* (EN), Risø National Laboratory, Roskilde, Denmark.

Mission

To promote an innovative and environmentally sustainable technological development within the areas of energy, industrial technology and bioproduction through research, innovation and advisory services.

Vision

Risø's research **shall extend the boundaries** for the understanding of nature's processes and interactions right down to the molecular nanoscale.

The results obtained shall **set new trends** for the development of sustainable technologies within the fields of energy, industrial technology and biotechnology.

The efforts made **shall benefit** Danish society and lead to the development of new multi-billion industries.